Available online at www.sciencedirect.com
SCIENCE DIRECT
Journal of Power Sources 156 (2006) 355–368
JOURNAL OF POWER SOURCES
www.elsevier.com/locate/jpowsour

Predicting the transient response of a serpentine flow-field PEMFC I. Excess to normal fuel and air

S. Shimpalee [a], W.-k. Lee [a], J.W. Van Zee [a,*], H. Naseri-Neshat [b]

[a] *Department of Chemical Engineering, University of South Carolina, Columbia, SC 29208, USA*
[b] *Department of Mechanical Engineering Technology, South Carolina State University, Orangeburg, SC 29117, USA*

Received 26 April 2005; accepted 20 May 2005
Available online 12 July 2005

Abstract

A three-dimensional numerical simulation of the transient response of a polymer electrolyte membrane fuel cell (PEMFC) subjected to a variable load is presented. The model parameters are typical for a laboratory-scale cell with a serpentine flow path and a 10 cm^2 reactive area. The simulation uses a commercial computational fluid dynamics (CFD) solver modified to include the electrochemical behavior. The predictions are based on an isothermal set of equations and include transient responses of the cell in terms of local distributions of the current density and gas mole fractions. The predictions show transients in the current density that overshoot the final state value when the cell voltage is abruptly changed from 0.7 to 0.5 V for fixed excess initial stoichiometric flowrates. The fixed flowrates are excess because they correspond to stoichiometries of 2.6 and 4.4 at 0.7 V for the 0.35 A/cm^2 predicted initial current density. The percent overshoot decreases with the rate of voltage change and it is shown to change with anode gas flow rates. Also the magnitude of this overshoot and undershoot can be adjusted by changing the rate of voltage change and the operating conditions. The overshoot behavior for these excess stoichiometric flowrates is shown to depend on changes in the oxygen mole fraction distributions.

Keywords: PEM; Fuel cells; Membrane electrode assembly; Electric vehicle; Dynamic response; Overshoot

1. Introduction

The control, design, and optimum operation of polymer electrolyte membrane fuel cells (PEMFCs) will require an understanding of its dynamics when there are changes in either current, voltage, or power. These dynamics would be important for power conditioning in residential applications and for automotive systems performing in a Federal Urban Driving Scenario. While some of these dynamics could be determined from experiments, a model capable of predicting the transient response would be useful in the design flow fields and for optimization of control schemes. We are particularly interested in overshoot behavior because recent experiments in our laboratory [1–3] indicate the possibility of overshoot behavior dependent on the rate of voltage change, and stoichiometry.

As a guide for simple one-dimensional (1D) and two-dimensional (2D) models that may be developed in the future, we present here a three-dimensional (3D) solution to the isothermal, time-dependent phenomena that includes Navier–Stokes equations for the flow channel and diffusion layers of a serpentine flow field and the interaction of theses equations with anode and cathode kinetics, and the water balance throughout the cell. It is important to note that simpler models (i.e., 2D transient) could not accurately provide predictions of the serpentine flow-field. Commonly use to test membrane electrode assemblies (MEA). To obtain this solution, the 3D model of Shimpalee et al. [4,5] was extended by including the time dependent analysis of a 10-cm^2 reactive area. This set of equations, as shown below, does not account explicitly for the condensation of water vapor resulting from the local partial pressure exceeding the saturation

* Corresponding author. Tel.: +1 803 777 2285; fax: +1 803 777 8265.
E-mail address: vanzee@engr.sc.edu (J.W. Van Zee).

0378-7753/$ – see front matter © 2005 Elsevier B.V. All rights reserved.
doi:10.1016/j.jpowsour.2005.05.073

pressure of water, but rather it calculates the activity of water in the gas phase and allows the analyst to manually turn off the reaction in the cells where the thickness of condensed liquid restricts mass transfer to the catalyst. Recent steady-state versions of this model [6–8] account for this water phase change and include the energy balance to predict temperature changes, but under some operational conditions liquid water does not significantly affect the performance of the cell and computational time can be saved by neglecting these phase changes. Hence, an isothermal single-phase approximation is used here.

The equations of this paper and the results discussed below can be related to previous works. For example, Um et al. [9] presented similar equations for their 3D model and applied those to their straight channel geometries. They used their own code and the equation solver was not specified. Recently Wang and Wang [10] showed dynamic study on PEMFC using commercial CFD code. However, their geometry was single straight channel flow field that is not normally used in fuel cell application, therefore the effect of pressure driven flow underneath the gas diffusion layers has been ignored. In the results presented below we also used a commercially available computational fluid dynamics (CFD) solver and we had to supply subroutines to account for the electrochemical reactions of hydrogen and oxygen for source terms in the transport equations. The complete equations are solved with a control volume based discretization of the computational domain to obtain the velocity and pressure distribution in the flow channels and the gas diffusion layers for every time interval.

In contrast to the transient analysis presented here and recent paper from reference [10], preceding modeling studies have focused on the steady state behavior of the fuel cell. Some models considered only 1D simulations [11–13], several models concentrated on 2D flow with transport of the reactants and products in the flow channels and across the membranes [14–21], and recent models put emphasis on the 3D simulations [4–10]. Some of These works have been reviewed by Shimpalee et al. [22]. One recent 1D transient model has been presented and transient measurements of the voltage as the current was changed were used to estimate parameter of a MEA. However, that model was not used to explain changing in the overshoot behavior with stoichiometry. It may also to note that the non-isothermal form of the model presented here has been verified with water balance measurement recently [7].

2. Model development

In this study, the 3D model of Shimpalee and coworkers [4,5] is extended by including the accumulation (time dependent) term. Thus, this is a transient, 3D, isothermal, single phase, and multi-species investigation of a single PEM fuel cell with twenty serpentine channels. Again, an isothermal set of equations is used to increase computational speed and to provide a basis of comparison for future work. The flow path consists of a serpentine gas channel and the details of the computational domain have been shown previously, [5,7]. Fig. 1 also shows the channel geometry and associated coordinate system. A thin membrane electrode assembly is sandwiched between anode and cathode diffusion layers. Fig. 2 shows more details of the computational domain, which consists of the anode flow channel, the anode diffusion layer, the MEA, the cathode diffusion layer, and the cathode flow channel. Fig. 2 further shows different z-locations that are used in defining source terms (see Table 1 for a list of symbols and Tables 2 and 3 for the equations used in this paper). The species considered are hydrogen, oxygen, nitrogen, and water vapor. The fuel cell operation is characterized as gas transport and transformation of one species to the other. The hydrogen from the anode flow channel is transported through the diffusion layer toward the membrane. Hydrogen molecules are dissociated to protons and electrons in the catalyst. The water that impregnates the MEA hydrates the protons and it is transported by both electro-osmosis and diffusion according to Eq. (15) of Table 3. The air mixture in the cathode channel is transported through the diffusion layer toward the membrane where oxygen reacts with protons. The water activity in the membrane is simulated by surface-

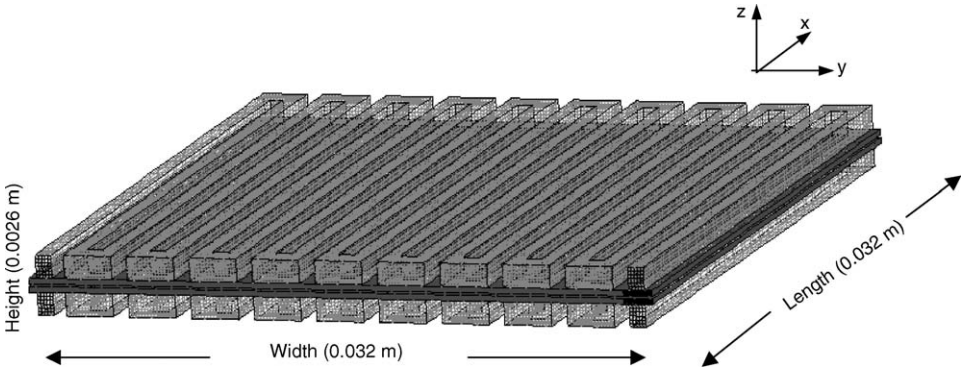

Fig. 1. The picture shows actual flow-field plate with the gas channel and its geometry model. There are 20 straight channels connected in a serpentine fashion. Anode and cathode side flow channels are symmetric and placed properly aligned on top of each other [2,3].

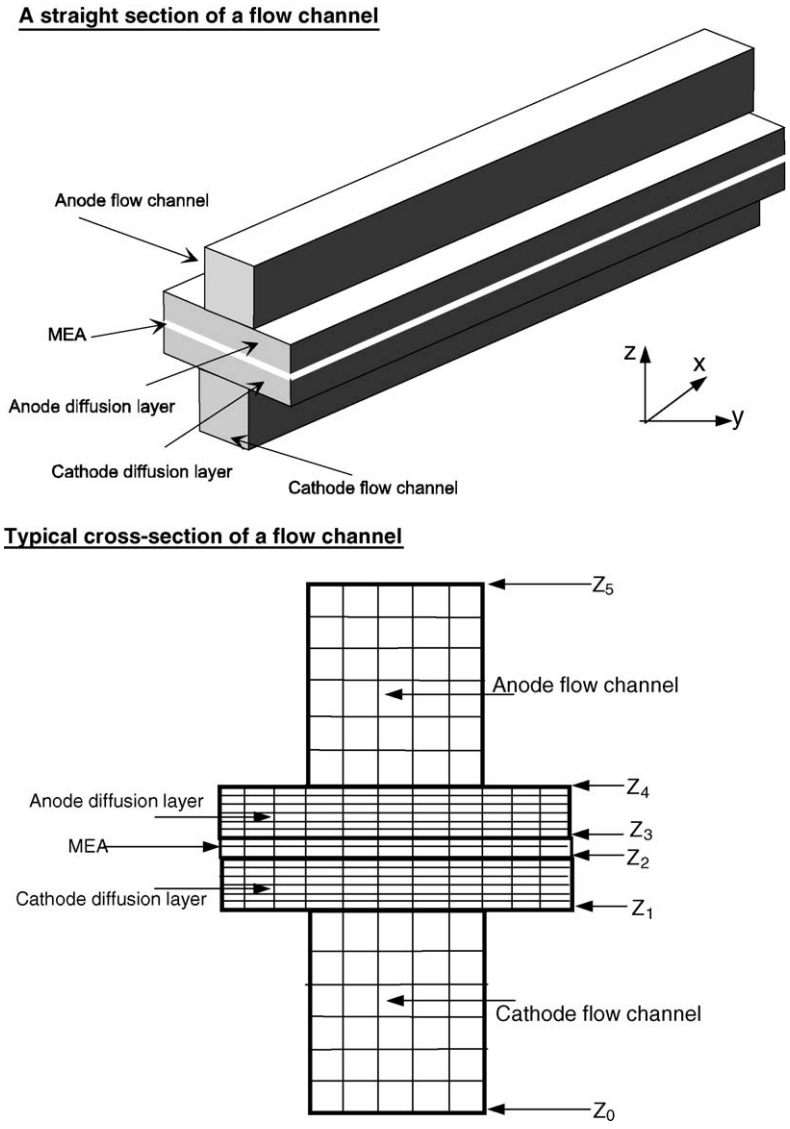

Fig. 2. The detail of computational domain and grid arrangement used in this model [2,3]. Note the number of volume elements used in references [2,3] and shown in this figure is greater in the z-direction than the number used here as discussed in the text.

based source terms in the control volumes in contact with the membrane.

Table 2 shows the model equations. The steady state aspects of these equations have been discussed elsewhere [4,5,22]. It may be important to note that the time dependent conservation of mass equation (Table 2, Eq. (1)) in the 3D flow domain is modified to include the electrochemical reactions of a fuel cell by using the respective source terms, S_m, specified through Eqs. (7) and (9)–(12) of Table 2. Note that the source terms are zero in most of the computational domain. These terms corresponds to the consumption of hydrogen in the anode, and the consumption of oxygen and production of water in the cathode. The flux of water is also included as a source term at the anode and cathode (i.e., Eqs. (10) and (12)) by accounting for the diffusion, water content in the membrane, and electro-osmotic drag coefficient as defined by Eqs. (15)–(17) of Table 3. Note that Eqs. (15)–(17) of Table 3 were verified with water balance measurement [7]. Note also that Eq. (17) approximates the data of Springer and coworkers [23] since $\lambda = 11$ @ $n_d = 0.9$. Also note that Eq. (17) and there reference [23] differ from the data presented by Fuller and Newman [24] where in there Fig. 4, n_d (their ξ) is constant at 1.2 until $\lambda = 4$. These equations will vary with membrane and ionomer as characterized by the equivalent weight and density in Eq. (19).

The species transport equations (Eqs. (3)–(6) of Table 2) are solved for the mass flow rates of the hydrogen, water, and oxygen species based on the mixture component velocities, u, v, and w, and the diffusion mass fluxes $J_{\xi,l}$ for every time step. The species binary diffusion coefficients are calculated as shown by Eq. (14) in Table 3. Fuller and Newman [14] integrate the flux expression for the diffusion of water through the membrane whereas references [13,15,17]

Table 1
List of symbols

a_K	Activity of water in stream K (dimensionless)
A_{cv}	Specific surface area of the control volume (cv) (m^{-1})
C	Condensation rate (s^{-1})
C_{wK}	Concentration of water vapor at K interface of the membrane (mol m^{-3})
$D_{n,j}$	Binary diffusion coefficient of species n in mixture j (m^2 s^{-1})
D_w	Diffusion coefficient of water (m^2 s^{-1})
F	Faraday constant (96487C mol-of-electrons^{-1})
I	Local current density (A m^{-2})
I_o	Exchange current density (A m^{-2})
$m_{n,K}$	Mass fraction of the species n in stream K (dimensionless)
$M_{m,dry}$	Equivalent weight of a dry membrane (kg mol^{-1})
M_n	Molecular weight of species n (kg mol^{-1})
$mass_n$	Mass of species n (kg)
n_d	Electro-osmotic drag coefficient (number of water molecules carried per proton)
$P^{sat}_{w,K}$	Vapor pressure of water in stream K (Pa)
P	Pressure (Pa)
P_n	Partial pressure of species n (pa)
Q	Volume flow rate (m^3/s)
R	Universal gas constant (8.314 J mol^{-1} K^{-1})
S	Source term
t	Time (s)
t_m	Membrane thickness (m)
T	Temperature (K)
u, v, w	Velocities in x, y, and z directions, respectively (m s^{-1})
V_{oc}	Cell open-circuit voltage (V)
V_{cell}	Cell voltage (V)
x	Channel length measured from anode inlet (m)
$X_{w,K}$	Mole fraction of water in stream K
Greek symbols	
α	Net water flux per proton flux
β_ξ	Permeability in the ξ direction
η	Total overpotential for oxygen and hydrogen reactions (V)
λ	Water content in the membrane
μ	Dynamic viscosity (kg s m^{-2})
$\rho_{m,dry}$	Density of a dry membrane (kg m^{-3})
ρ	Density of the mixture (kg m^{-3})
$\sigma_{\underline{m}}$	Membrane conductivity (ohm^{-1} m^{-1})
Subscripts and superscripts	
a	Anode
c	Cathode
CO_2	Carbon dioxide
e	Electrochemical reaction
H_2	Hydrogen
K	Anode or cathode streams
N_2	Nitrogen
O_2	Oxygen
v	Vapor
w	Water
sat	Saturated
ξ	Dummy variable for direction x, y, or z

assumed a linear gradient as shown by Eq. (15). In this study, the diffusion coefficient of each species in the diffusion layer was reduced arbitrarily by 50% to account for the effect of porosity and pore-tortuosity. The flux of water through the membrane is critical to the predictions and here we have used the same equation for water content in the membrane as given in Springer et al. [11]. Eq. (17) gives relationship between the electro-osmotic drag coefficient and water content in the membrane. This equation is arrived at by curve-fitting the values of water content in the membrane and electro-osmotic drag coefficient presented in Springer et al. [11]. The diffusion coefficient given in Eq. (18) in Table 3 is taken from Nguyen and White [15].

The expressions for water concentration at the anode and cathode sides, $C_{w,a}$ and $C_{w,c}$, are calculated according to Eq. (19), and the activity of water is also defined in Table 3. Moreover, the effects of local hydrogen and oxygen overpotentials are accounted as shown in Eq. (23). It is important to note that the source terms in Table 2 correspond to the control volume and not the boundary conditions at the anode or cathode interfaces. For the correct determination of the concentrations and activities at the membrane-diffusion layer interface, the mole fraction for each species used in these equations is extrapolated to the membrane surface.

It is important to note that here the transient predictions below assume negligible capacitance per unit area. That is the transient current is the sum of a Faraday current density as described by Eq. (21) of Table 3 and a charging current density, $I_c(x,y)$. This charging current is related to the change in overpotential, $\eta(x,y)$:

$$I_c(x, y) = C\frac{d\eta(x, y)}{dt}$$

2.1. Numerical procedure

A control volume technique based on Star-CD version 3.2 commercial flow solver was used to solve the coupled time dependent governing equations. Since we neglect $I_c(x,y)$ the predictions shown below would apply to Pt electrode by not a Pt/Ru electrode since Ru has a large C. Several subroutines were added to calculate and account for the source terms, permeability, electrochemical reactions, and flux of protons and water across the membrane according to the equations of Tables 2 and 3.

Figs. 1 and 2 show the geometry of fuel cell modeled in this work, which consists of two flow channels separated by diffusion layers and MEA. There are twenty serpentine passes in the flow path, so that the flow is approximately sixty centimeters long in the axial direction with 0.1 cm(height) × 0.08 cm (width) cross-section flow area. Each diffusion layer has dimension of 0.025 cm (height) × 3.20 cm (width) × 3.20 cm (length). A total of 34 28 cells × 200 28 cells × 28 cells (elements) were used to model the fuel cell. That is, we use 34 cells × 200 cells × 6 cells for both anode and cathode diffusion layers and 34 cells × 200 cells × 6 cells for both anode and cathode flow channels, 34 cells × 200 cells × 2 cells for the MEA, and 34 cells × 200 cells × 2 cells for caps on the flow channels corresponding to the graphite current collectors.

The solution procedure used in this commercial flow solver is based on a SIMPLE algorithm [25]. For every time

Table 2
Governing equations and source terms

Governing equations	Mathematical expressions		Non-zero volumetric source terms and location of application (see Fig. 2)	
Conservation of mass	$\frac{\partial \rho}{\partial t} + \frac{\partial(\rho u)}{\partial x} + \frac{\partial(\rho v)}{\partial y} + \frac{\partial(\rho w)}{\partial z} = S_{\mathrm{m}}$	(1)	$S_{\mathrm{m}} = S_{\mathrm{H_2}} + S_{\mathrm{aw}}$ at $z = z_3$ $S_{\mathrm{m}} = S_{\mathrm{O_2}} + S_{\mathrm{cw}}$ at $z = z_2$	(7)
Momentum transport	$\frac{\partial(\rho u)}{\partial t} + u\frac{\partial(\rho u)}{\partial x} + v\frac{\partial(\rho u)}{\partial y} + w\frac{\partial(\rho u)}{\partial z} = -\frac{\partial P}{\partial x} + \frac{\partial}{\partial x}\left(\mu\frac{\partial u}{\partial x}\right) + \frac{\partial}{\partial y}\left(\mu\frac{\partial u}{\partial y}\right) + \frac{\partial}{\partial z}\left(\mu\frac{\partial u}{\partial z}\right) + S_{px}$ $\frac{\partial(\rho v)}{\partial t} + u\frac{\partial(\rho v)}{\partial x} + v\frac{\partial(\rho v)}{\partial y} + w\frac{\partial(\rho v)}{\partial z} = -\frac{\partial P}{\partial y} + \frac{\partial}{\partial x}\left(\mu\frac{\partial v}{\partial x}\right) + \frac{\partial}{\partial y}\left(\mu\frac{\partial v}{\partial y}\right) + \frac{\partial}{\partial z}\left(\mu\frac{\partial v}{\partial z}\right) + S_{py}$ $\frac{\partial(\rho w)}{\partial t} + u\frac{\partial(\rho w)}{\partial x} + v\frac{\partial(\rho w)}{\partial y} + w\frac{\partial(\rho w)}{\partial z} = -\frac{\partial P}{\partial z} + \frac{\partial}{\partial x}\left(\mu\frac{\partial w}{\partial x}\right) + \frac{\partial}{\partial y}\left(\mu\frac{\partial w}{\partial y}\right) + \frac{\partial}{\partial z}\left(\mu\frac{\partial w}{\partial z}\right) + S_{pz}$	(2)	$S_{px} = -\frac{\mu u}{\beta_x}$; $S_{py} = -\frac{\mu v}{\beta_y}$; $S_{pz} = -\frac{\mu w}{\beta_z}$ at $z_1 \le z \le z_4$	(8)
Hydrogen transport (anode side)	$\frac{\partial(\rho m_{\mathrm{H_2}})}{\partial t} + u\frac{\partial(\rho m_{\mathrm{H_2}})}{\partial x} + v\frac{\partial(\rho m_{\mathrm{H_2}})}{\partial y} + w\frac{\partial(\rho m_{\mathrm{H_2}})}{\partial z} = \frac{\partial(J_{x,\mathrm{H_2}})}{\partial x} + \frac{\partial(J_{y,\mathrm{H_2}})}{\partial y} + \frac{\partial(J_{z,\mathrm{H_2}})}{\partial z} + S_{\mathrm{H_2}}$	(3)	$S_{\mathrm{H_2}} = -\frac{I(x,y)}{2F} M_{\mathrm{H_2}} A_{\mathrm{cv}}$ at $z = z_3$	(9)
Water transport (anode side)	$\frac{\partial(\rho m_{\mathrm{aw}})}{\partial t} + u\frac{\partial(\rho m_{\mathrm{aw}})}{\partial x} + v\frac{\partial(\rho m_{\mathrm{aw}})}{\partial y} + w\frac{\partial(\rho m_{\mathrm{aw}})}{\partial z} = \frac{\partial(J_{x,\mathrm{aw}})}{\partial x} + \frac{\partial(J_{y,\mathrm{aw}})}{\partial y} + \frac{\partial(J_{z,\mathrm{aw}})}{\partial z} + S_{\mathrm{aw}}$	(4)	$S_{\mathrm{aw}} = -\frac{\alpha(x,y)}{F} I(x,y) M_{\mathrm{H_2O}} A_{\mathrm{cv}}$ at $z = z_3$	(10)
Oxygen transport (cathode side)	$\frac{\partial(\rho m_{\mathrm{O_2}})}{\partial t} + u\frac{\partial(\rho m_{\mathrm{O_2}})}{\partial x} + v\frac{\partial(\rho m_{\mathrm{O_2}})}{\partial y} + w\frac{\partial(\rho m_{\mathrm{O_2}})}{\partial z} = \frac{\partial(J_{x,\mathrm{O_2}})}{\partial x} + \frac{\partial(J_{y,\mathrm{O_2}})}{\partial y} + \frac{\partial(J_{z,\mathrm{O_2}})}{\partial z} + S_{\mathrm{O_2}}$	(5)	$S_{\mathrm{O_2}} = -\frac{I(x,y)}{4F} M_{\mathrm{O_2}} A_{\mathrm{cv}}$ at $z = z_2$	(11)
Water transport (cathode side)	$\frac{\partial(\rho m_{\mathrm{cw}})}{\partial t} + u\frac{\partial(\rho m_{\mathrm{cw}})}{\partial x} + v\frac{\partial(\rho m_{\mathrm{cw}})}{\partial y} + w\frac{\partial(\rho m_{\mathrm{cw}})}{\partial z} = \frac{\partial(J_{x,\mathrm{cw}})}{\partial x} + \frac{\partial(J_{y,\mathrm{cw}})}{\partial y} + \frac{\partial(J_{y,\mathrm{cw}})}{\partial y} + S_{\mathrm{cw}}$	(6)	$S_{\mathrm{cw}} = \frac{1 + 2\alpha(x,y)}{2F} I(x,y) M_{\mathrm{H_2O}} A_{\mathrm{cv}}$ at $z = z_2$	(12)

Table 3
Equations for modeling electrochemical effects

Diffusion mass flux of species l in ξ direction	$J_{i,l} = -\rho D_{i,l} \dfrac{\partial m_{\mathrm{K},l}}{\partial \xi}$ (13)
Binary diffusion coefficient [26]	$\dfrac{PD_{i,j}(x,y)}{(P_{c-i} \times P_{c-j})^{1/3}(T_{c-i} \times T_{c-j})^{5/12}((1/M_i)+(1/M_j))^{1/2}} = 3.64 \times 10^{-8} \left(\dfrac{T_{\mathrm{cell}}}{\sqrt{T_{c-i} \times T_{c-j}}} \right)^{2.334}$ (14)
Net water transfer coefficient per proton	$\alpha(x,y) = n_{\mathrm{d}}(x,y) - \dfrac{F}{I(x,y)} D_W(x,y) \dfrac{(C_{\mathrm{wc}}(x,y) - C_{\mathrm{wa}}(x,y))}{t_{\mathrm{m}}}$ (15)
Water content in the membrane	$\lambda = 0.043 + 17.81a_{\mathrm{a}} - 39.85a_{\mathrm{a}}^2 + 36.0a_{\mathrm{a}}^3; \quad 0 < a_{\mathrm{a}} \le 1$ $\lambda = 14 + 1.4(a_{\mathrm{a}} - 1); \quad 1 < a_{\mathrm{a}} \le 3$ (16)
Electro-osmotic drag coefficient	$n_{\mathrm{d}} = 0.0029\lambda^2 + 0.05\lambda - 3.4 \times 10^{-19}$ (17)
Water diffusion coefficient	$D_{\mathrm{w}} = n_{\mathrm{d}} 5.5 \times 10^{-11} \exp\left[2416\left(\dfrac{1}{303} - \dfrac{1}{T}\right)\right]$ (18)
Water concentration for anode and cathode surfaces of the MEA	$C_{\mathrm{wK}}(x,y) = \dfrac{\rho_{\mathrm{m,dry}}}{M_{\mathrm{m,dry}}}(0.043 + 17.8a_{\mathrm{K}} - 39.8a_{\mathrm{K}}^2 + 36.0a_{\mathrm{K}}^3); \quad a_{\mathrm{K}} \le 1$ $C_{\mathrm{wK}}(x,y) = \dfrac{\rho_{\mathrm{m,dry}}}{M_{\mathrm{m,dry}}}(14 + 1.4(a_{\mathrm{K}} - 1)); \quad \text{for} \quad a_{\mathrm{K}} > 1, \quad \text{where} \quad K = a \quad \text{or} \quad c$ (19)
Water activity	$a_{\mathrm{K}} = \dfrac{X_{\mathrm{w,K}} P(x,y)}{P_{\mathrm{w,K}}^{\mathrm{sat}}}$ (20)
Local current density	$I(x,y) = \dfrac{\sigma_{\mathrm{m}}(x,y)}{t_{\mathrm{m}}}\{V_{\mathrm{oc}} - V_{\mathrm{cell}} - \eta(x,y)\}$ (21)
Local membrane conductivity	$\sigma_{\mathrm{m}}(x,y) = \left(0.00514 \dfrac{M_{\mathrm{m,dry}}}{\rho_{\mathrm{m,dry}}} C_{\mathrm{wa}}(x,y) - 0.00326\right) \exp\left(1268\left(\dfrac{1}{303} - \dfrac{1}{T}\right)\right) \times 10^2$ (22)
Local overpotential	$\eta(x,y) = \dfrac{\mathrm{RT}}{0.5F} \ln\left[\dfrac{I(x,y)P(x,y)}{I_{0_{\mathrm{O_2}}} P_{\mathrm{O_2}}(x,y)}\right] + \dfrac{\mathrm{RT}}{0.5F} \ln\left[\dfrac{I(x,y)P(x,y)}{I_{0_{\mathrm{H_2}}} P_{\mathrm{H_2}}}\right]$ (23)
Viscosity of mixture	$\mu = \sum_i m_i \mu_i$ (24)

step, three momentum equations corresponding to three spatial coordinates are solved, followed by a pressure correction equation that corrects the mass balance. Species transport equations are solved after the bulk flow calculation. The mixture properties at each control volume are calculated based on the local species content. The anode side gas mixture contains hydrogen and water vapor. On the other hand, the cathode side gas mixture contains oxygen, water vapor, and nitrogen. Therefore, the density and viscosity of the two flow channels are different and vary from one location to the other. Note that the solution procedure for the time-dependent predictions is a fully implicit scheme [25]. Therefore, the newly calculated values of the variables prevail throughout the time step Δt. We tested the results to be sure that they were independent of time step size. That is for example we stepped from 0.02 to 0.04 s first with a Δt of 0.001 s and then with a Δt of 0.005 s and the results were the same to within 5%. Also, during steady state simulations, a separate grid independence test was performed by increasing and decreasing the number of the grid cells on a straight channel. The number of grid cell was decreased and increased by 50% of the base case, and predicted results were compared with the base result. The results were less than 2% different from each other.

3. Results and discussion

The effects of the rate of change in cell voltage on cell performance are studied for three different rates shown in Fig. 3. Condition #1 is a step change, and conditions #2 and #3 correspond to incremental changes with the time profiles detailed in Table 4. For most of predictions, operating flow

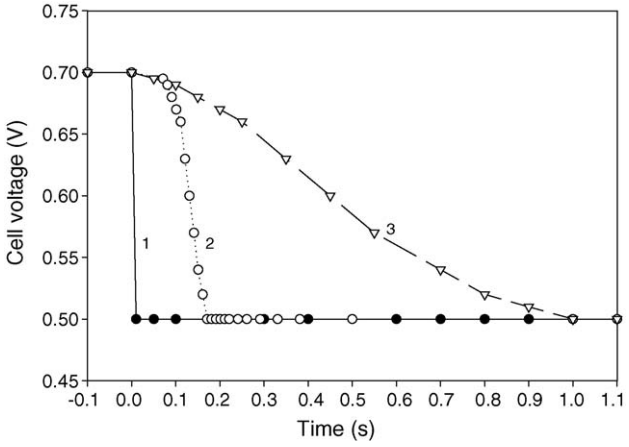

Fig. 3. Cell voltage changes with time used in this study. Condition 1 (●), a step change; condition 2 (◯), an increment change 1; condition 3 (▽), a slower increment change.

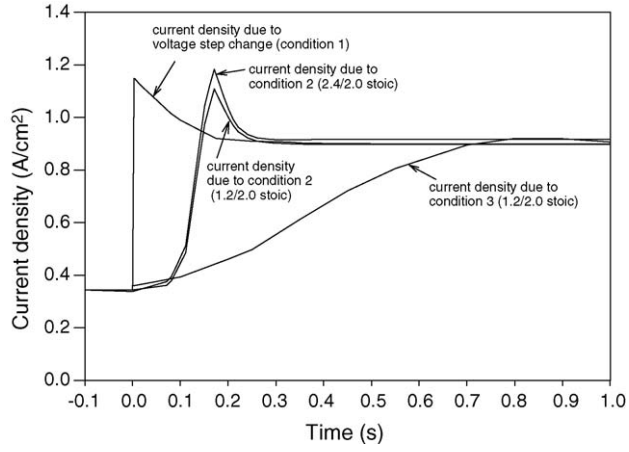

Fig. 4. Transient response of average current density between voltage step change and voltage increment change from 0.7 to 0.5 V.

rates for this study corresponded to flow rates that were 1.2 times greater than that required (by the measured current) for hydrogen (i.e., 20% excess hydrogen) and 2.0 time greater than that required for air (i.e., 100% excess air) at the cell voltage of 0.5 V. Thus, we call this a stoichiometric flow (stoic) of 1.2/2.0 (i.e., 1.2 for anode and 2.0 for the cathode). The anode and cathode flows were co-current and constant. The initial conditions correspond to steady state concentrations and velocity and pressure distributions at 0.5 V with a feed velocity of 2.6 m/s. This corresponds to an initial stoic of 2.6/4.4 at 0.7 V and a final stoic of ∼1.2/2.0 at 0.5 V. Thus,

Table 5
Inlet conditions, physical properties, and model parameters

Cell voltage	
Volts	0.5
Anode channel inlet conditions for stoich of 1.2	
Velocity ($m\,s^{-1}$)	2.6
Mole fraction of H_2	0.729
Mole fraction of H_2O	0.271
Dew point temperature (°C)	∼65
Cathode channel inlet conditions for stoich of 2.0	
Velocity ($m\,s^{-1}$)	9.9
Mole fraction of O_2	0.165
Mole fraction of N_2	0.622
Mole fraction of H_2O	0.213
Dew point temperature (°C)	∼57
Operating conditions	
Operating pressure (kPa)	101
Cell voltage (V)	0.5
Permeability of diffusion layer (m^2)	3.3×10^{-15}
Membrane thickness (μm)	50
Density of dry membrane ($kg\,m^{-3}$)	2000
Equivalent weight of a dry membrane ($kg\,mol^{-1}$)	1.1
Oxygen exchange current density ($A\,m^{-2}$)	140
Hydrogen exchange current density ($A\,m^{-2}$)	1000

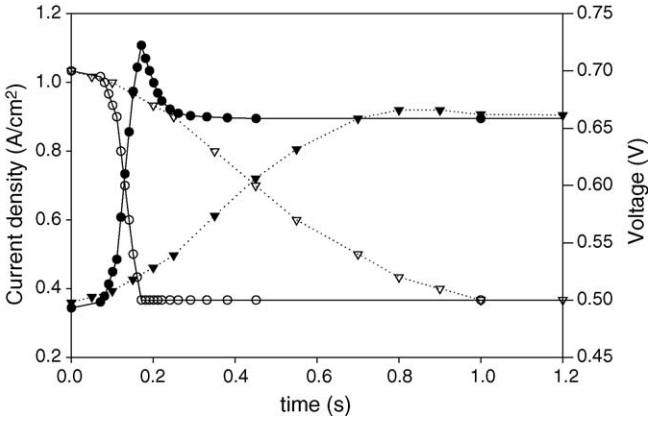

Fig. 5. Transient response of average current density with different voltage increment change from 0.7 to 0.5 V ((●) condition # 2 current density; (◯) condition # 2 voltage; (▼) condition # 3 current density; (▽) condition # 3 voltage).

we have an excess amount of fuel and air at time equal zero and a stoic of 1.2/2.0 at time equal to infinity. Other inlet conditions and physical properties are shown in Table 5. It is important to note that these conditions, the membrane is close to saturation (i.e., $\lambda = 10$) during all of the transient

Table 4
Voltage changes profiles

Condition #1	Time (s)	−0.10	0.00	0.01	0.05	0.10	0.20	0.30	0.40	0.50	0.60	0.70	0.80	0.90	1.00	1.10
	Voltage (V)	0.70	0.70	0.50	0.50	0.50	0.50	0.50	0.50	0.50	0.50	0.50	0.50	0.50	0.50	0.50
Condition #2	Time (s)	−0.10	0.00	0.07	0.08	0.09	0.10	0.11	0.12	0.13	0.14	0.15	0.16	0.17	0.18	1.10
	Voltage (V)	0.70	0.70	0.70	0.69	0.68	0.67	0.66	0.63	0.60	0.57	0.54	0.52	0.50	0.50	0.50
Condition #3	Time (s)	−0.1	0	0.05	0.1	0.15	0.2	0.25	0.35	0.45	0.55	0.7	0.8	0.9	1	1.1
	Voltage (V)	0.7	0.7	0.695	0.69	0.68	0.67	0.66	0.63	0.6	0.57	0.54	0.52	0.51	0.5	0.5

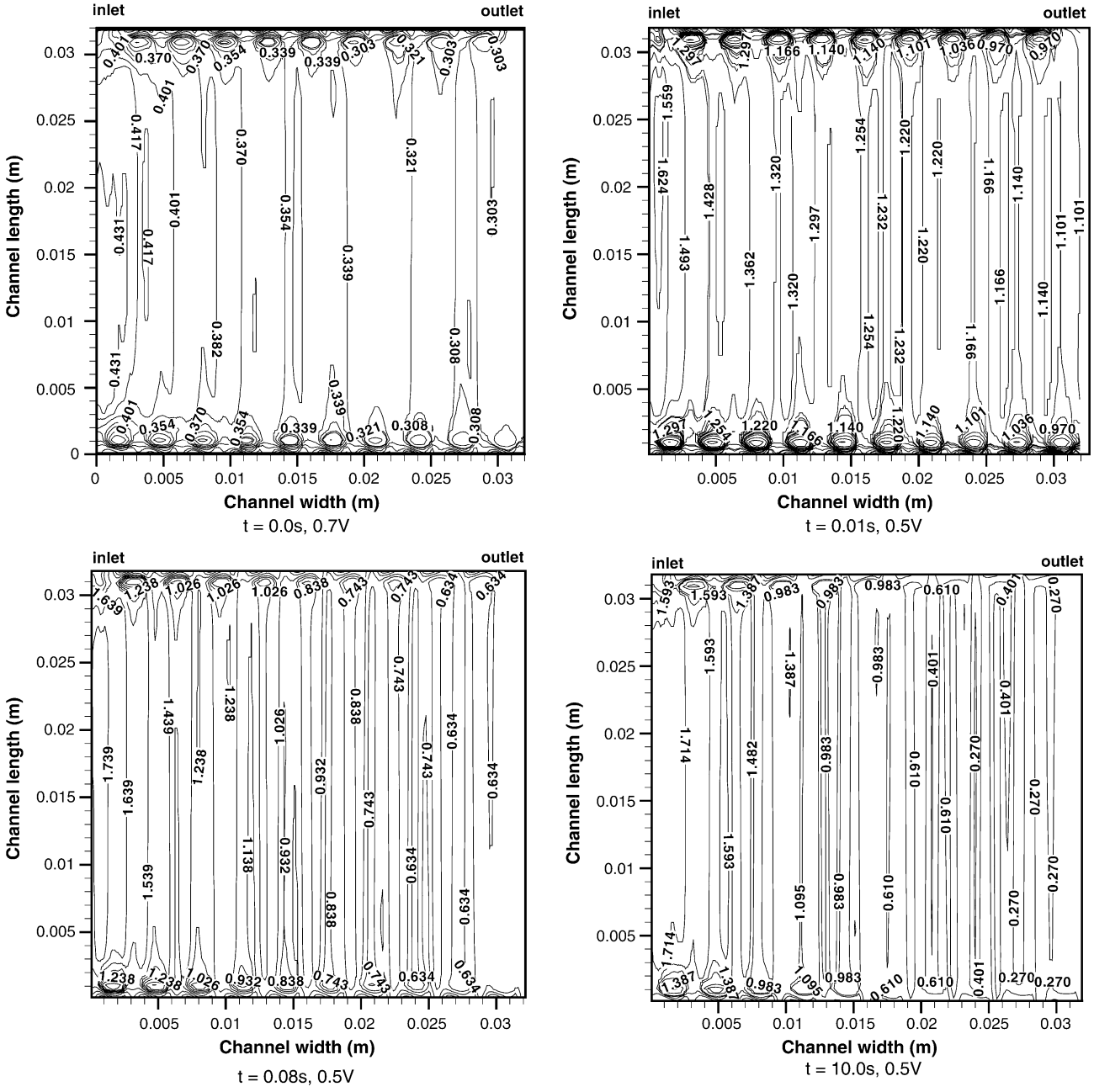

Fig. 6. Local transient current density (A/cm^2) contours at different times and cell voltages for a step voltage change condition (i.e., condition #1 of Fig. 3).

operation. This would not be the case if one is considering analysis of a start-up condition with a dry membrane. Thus, the fact that the time dependent for water in the membrane is approximately zero. This as discussed below that transient response is not a function of the changes in the membrane hydration. Note that our experiment for PRIMEA® MEAs indicates that the dew points of the anode and cathode are similar. The operating pressure is 101 kPa and cell temperature is constant at 70 °C. The membrane thickness used in this simulation is 50 μm.

Fig. 4 shows the response in the average current density when the changes in cell voltages are step and incremental as shown in Fig. 3. The cell voltage incremental change in this figure is for condition #2 of Fig. 3. Results are shown for two anode flow rates for the cell voltage change of condition #2, corresponding to stoics of 1.2 and 2.4 at 0.5 V. In this figure when the cell voltage is changed in one time step from 0.7 to 0.5 V, the average current density rapidly increases from 0.35 to 1.15 A/cm^2. Then the current density decreases with time and reaches steady state at $t = 0.17$ s with the current density of 0.90 A/cm^2. When the rate of voltage change is slower as for condition #2 with an anode stoic of 1.2, the current density increases initially and reaches the maximum average current density of 1.10 A/cm^2 at $t = 0.18$ s. Again, the current

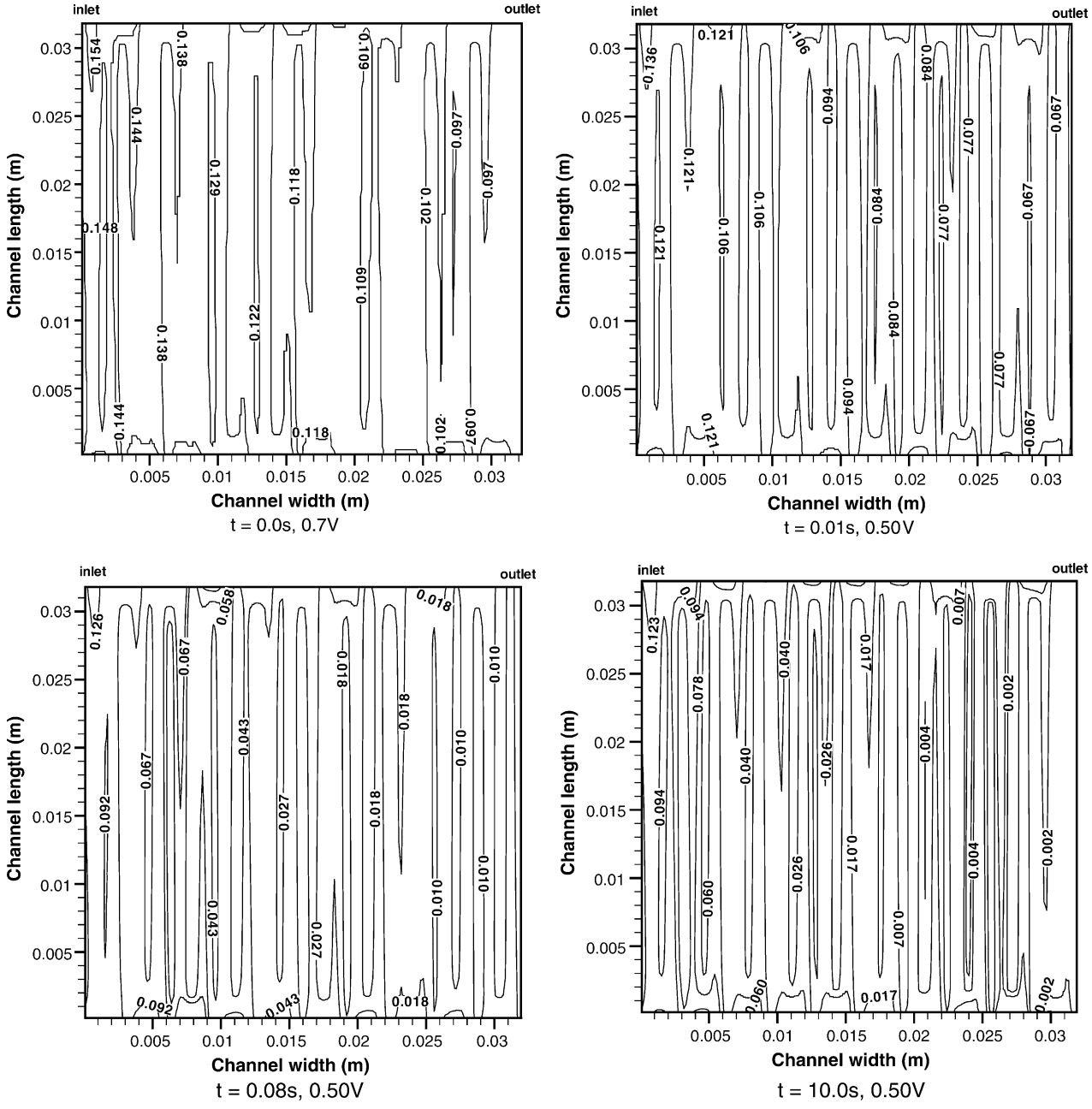

Fig. 7. Local transient oxygen mole fraction contours at different times and cell voltage for step voltage change condition #1.

density decreases until $t = 0.35$ s when it reaches the steady state value of 0.90 A/cm^2. When the anode stoic is increased to 2.4, the maximum current reaches 1.21 A/cm^2 at $t = 0.18$ s and the final steady state is 0.92 A/cm^2. Fig. 4 shows that the average current density overshoots its final steady state value for conditions #1 and #2 and that the peak of current overshoot depends on the rate of change of the voltage and the amount of gas flow rate. Higher gas flow rates result in greater current overshoot and a longer time to reach steady state.

Fig. 5 illustrates the transient current response with the voltage changes of conditions #2 and #3 of Fig. 3. This figure confirms that the magnitude of current overshoot is affected by the rate of change of cell voltage and it is consistent with the data of reference [1]. Note that it is difficult to experimental by obtaining 1 V/s change and hence the model provides useful insight to extreme conditions. For the rate of change of cell voltage corresponding to condition #3 in Fig. 3, the maximum average current density reaches 0.92 A/cm^2 at $t = 0.8$ s and cell voltage of 0.52 V. The current density reached steady state value of 0.90 A/cm^2 at $t = 1.0$ s. Additional computations not shown here verified that the overshoot could be eliminated completely if a proper function for the cell voltage change is implemented. This function can have a high rate of voltage

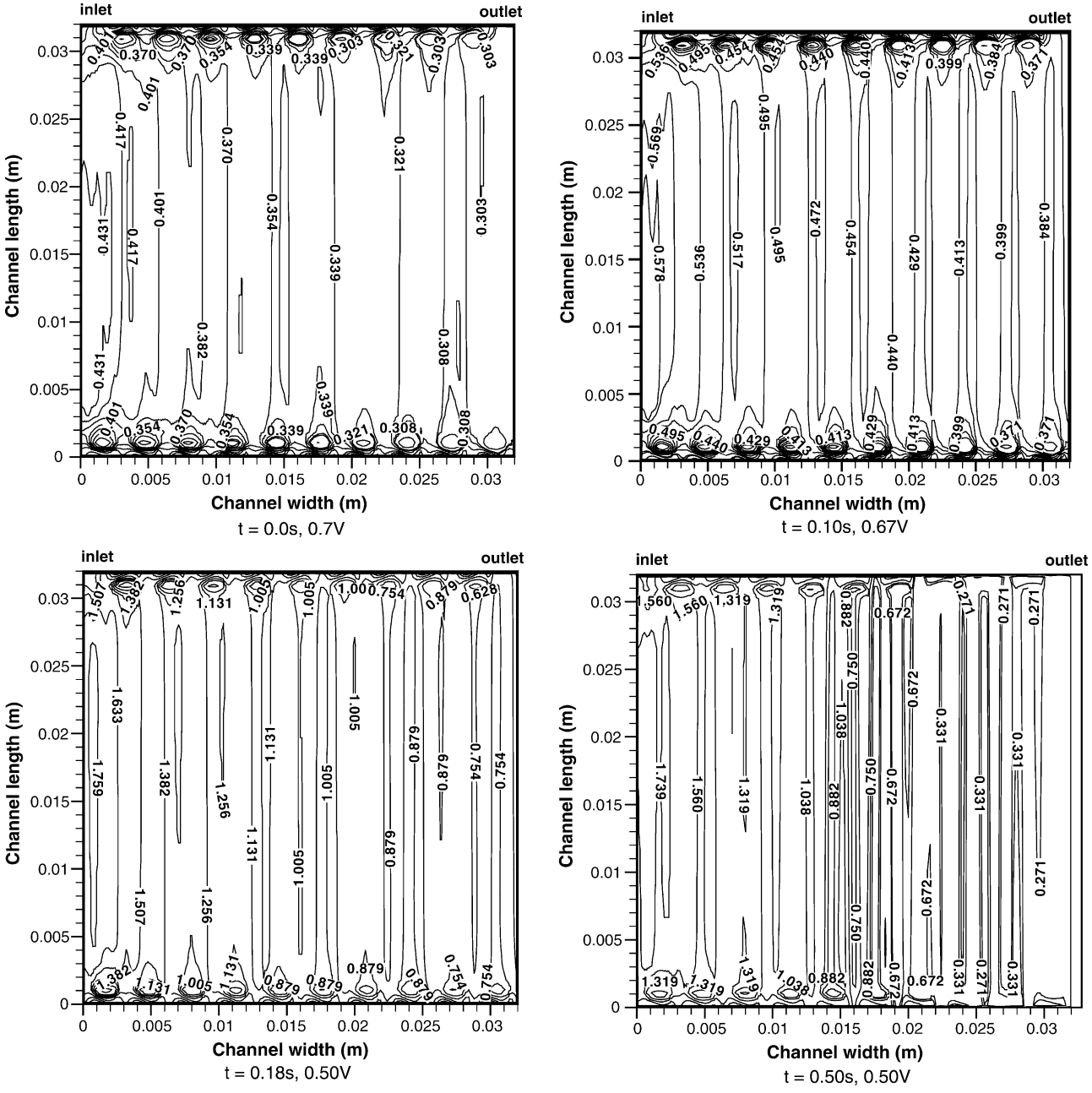

Fig. 8. Local transient current density (A/cm^2) contours at different times and cell voltages for increment voltage change condition #2. Here the maximum current occurs at $t = 0.18$ s.

change initially as long as the voltage change is small as the voltage approaches 0.5 V. The reasons for the overshoot are discussed below.

Fig. 6 shows the local current density on the membrane surface for four time steps and cell voltages for the step change. These figures show the spatial variations of local current density, which cannot be provided in 1D and 2D models. At the steady state corresponding to the cell voltage of 0.7 V and $t = 0.0$ s, the local current density is higher in the inlet region and decreases along the flow channel towards the outlet due to the lowering of anode activity of water by electroosmotic transport. The maximum and minimum local densities are 0.43 and 0.30 A/cm^2, respectively. The variation of current density is relatively small over the entire cell area. There are also current density variations at the channel bends and the higher current density is larger on the outside edges of the bends. This is because the sharp turns of the bends produce re-circulation zones around the outward corners (edges), resulting in larger velocities and hence higher gas concentrations at the inner corners than the outer corners. When the cell voltage is lowered to 0.5 V in 0.01 s, the local current density significantly increases over the membrane surface but the contour pattern is similar to the $t = 0.0$ s result. The highest local current density is 1.624 A/cm^2 and

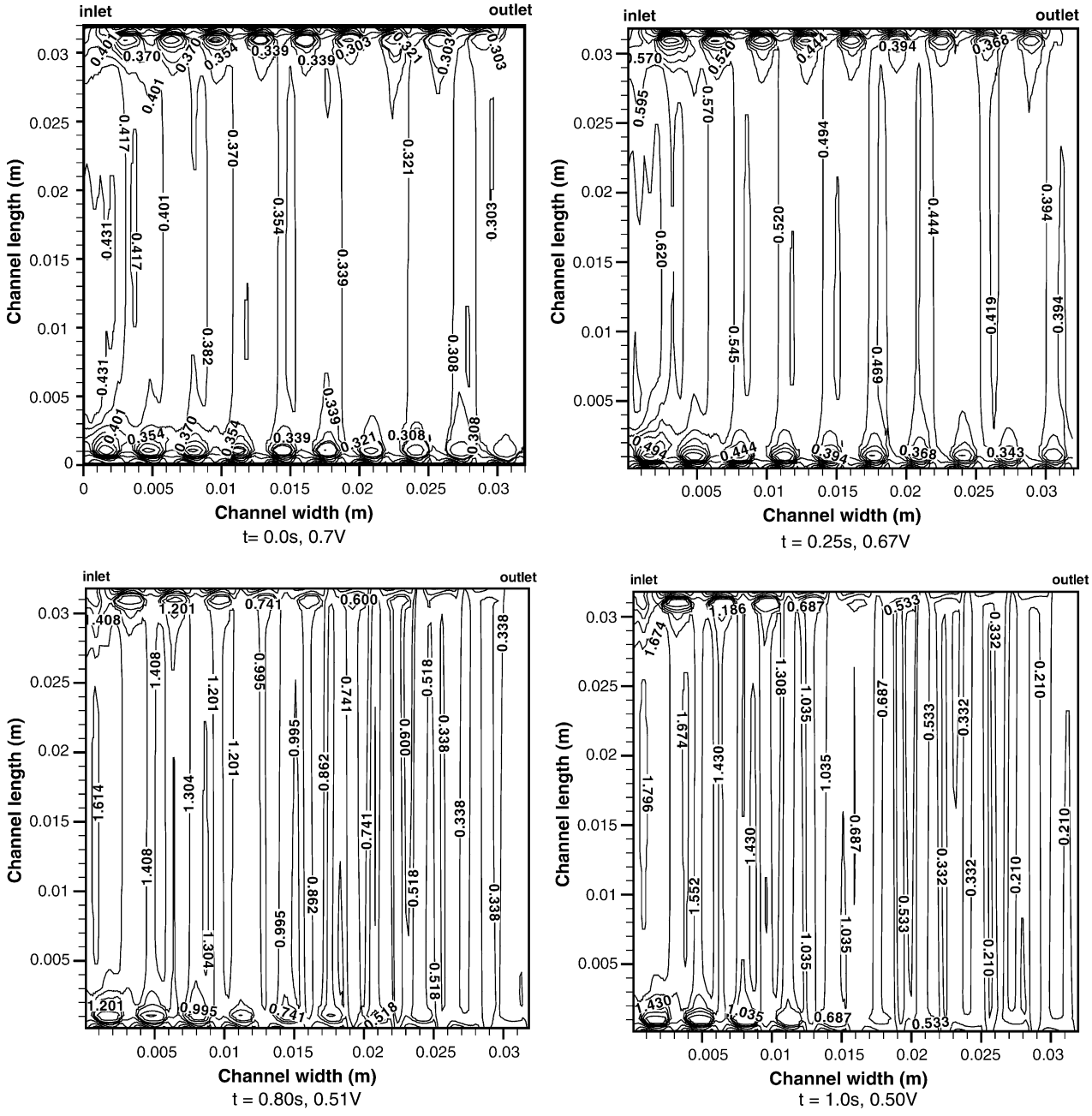

Fig. 9. Local transient current density (A/cm^2) contours at different times and cell voltages for increment voltage change condition #3. Here the maximum current occurs at $t = 0.8$ s.

the lowest value is 0.970 A/cm^2. As time increases, there is more non-uniformity of local current density distribution. At 0.08 s, the local current reduces considerably from the center of the membrane surface toward the outlet due to decreasing of oxygen concentration. The highest local current density is located around the inlet with a value of 1.74 A/cm^2 and the lowest local current density is at the outlet with a value of 0.63 A/cm^2. The figure for 10.0 s shows that at the final state the local current density varies from 1.71 to 0.27 A/cm^2 and that it decreases from the center region of the membrane surface towards the outlet region. This is because the high reaction rate regions consume the hydrogen and oxygen at the beginning of the channel and the down stream regions are depleted in reactants. Thus, the partial pressure of O_2 and H_2 change down the channel and under ribs even though λ and α are approximately constant. Again for other operating conditions especially those from a drier membrane would have different profiles and the model may need an accumulation term for the water balance. Here these are not necessary to illustrate the response to changes in the load.

Fig. 7 shows the transient local oxygen mole fraction contours on the membrane surface corresponding to the current

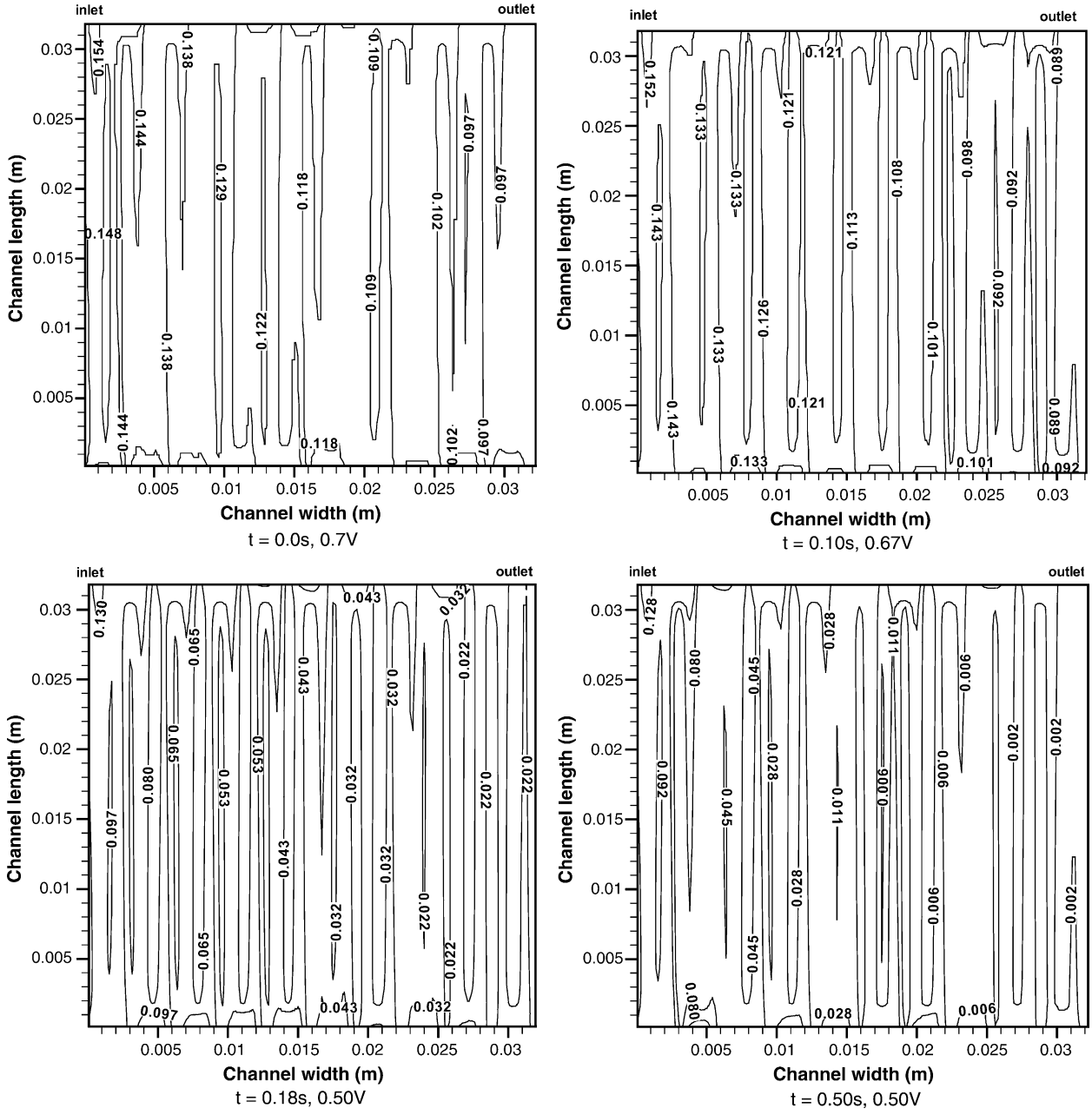

Fig. 10. Local transient oxygen mole fraction contours at different times and cell voltages for increment voltage change condition #2.

density of Fig. 6. These figures reveal that the local oxygen mole fraction patterns are consistent with the local current density contours. When the cell voltage is changed to 0.5 V with a time step of 0.01 s, the distribution of oxygen mole fraction becomes quite non-uniform and shows a rapid depletion towards the outlet regions of the membrane surface. The decrease of oxygen mole fraction in the inlet region of the membrane cell is about 18%, whereas the decrease is about 30% for the outlet region. Comparison of the four time step contours shows that the oxygen mole fraction in the inlet area of the membrane surface reaches its steady state value of 0.09 (a 38% reduction) in a time span of 0.08 s and that it reaches the steady value of 0.002 (a 98% reduction) over the last 50% of the membrane in 10 s. Under these conditions, there is not enough oxygen for reactions in the last section of the cell even though the over all stoich is 2.0 for the cathode. It may be important to note that the gradient of O_2 in the z direction (i.e., from the flow channel to the electrode surface) are much smaller than the changes from inlet to outlet for these value of the diffusion layer shown in Table 5.

There is a marked difference in transient local current density contours for the incremental change of cell voltage corresponding to conditions #2 and #3 of Fig. 3. These differences are discussed by comparing Figs. 8 and 9 with Fig. 6. At time $t = 0.0$ s the current density contour plot is the same

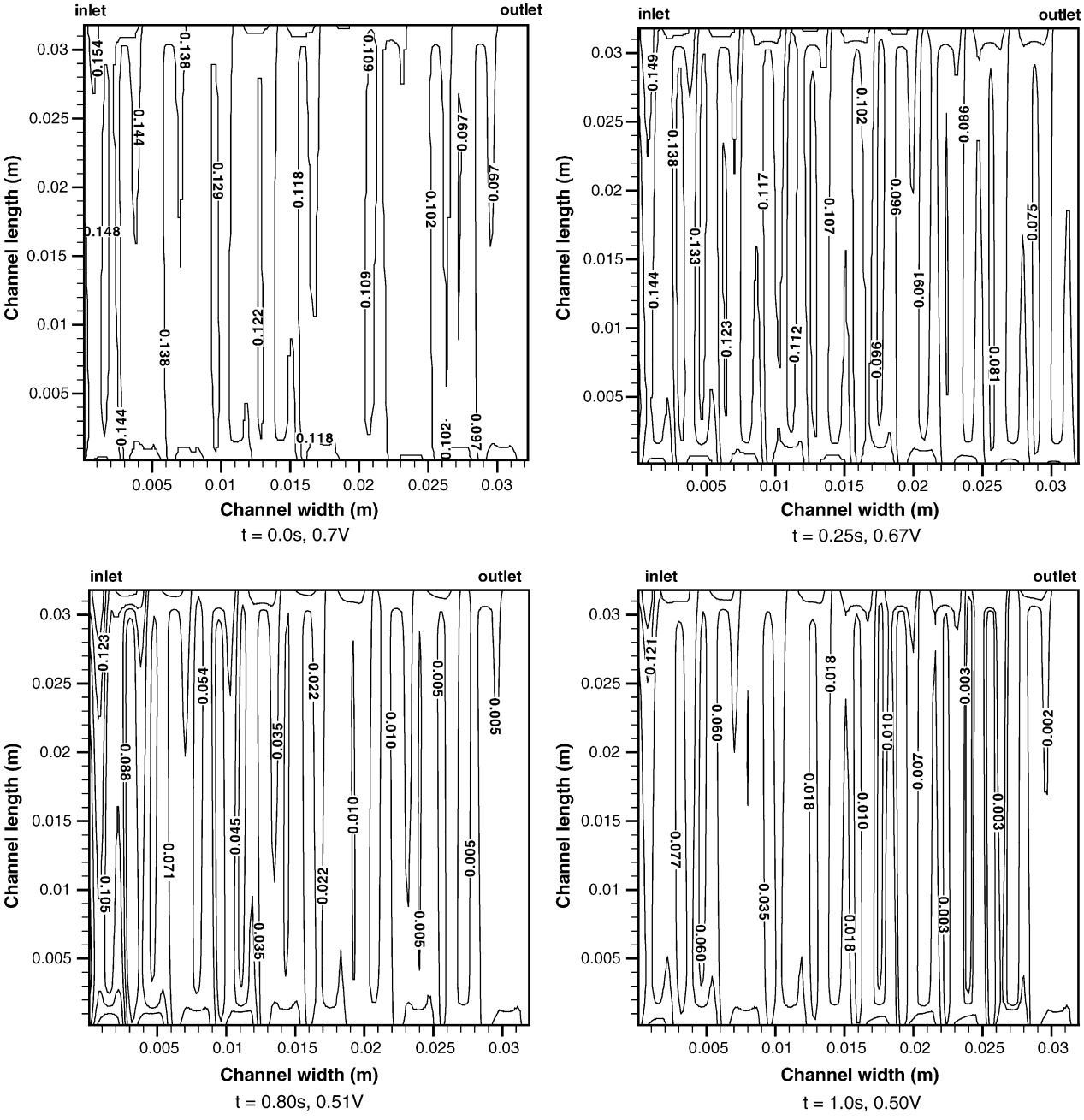

Fig. 11. Local transient oxygen mole fraction contours at different times and cell voltages for increment voltage change condition #3.

for all three conditions. Then for each time step each figure shows, in general, that the current density contours for gradually decrease from the inlet to the outlet. The major difference for the three conditions occurs at the time step at which the maximum overshoot occurs. The magnitude of the current density for all three conditions is comparable in the immediate inlet region of the cell but a slower rate of voltage changes allows the current density towards the outlet region to approach the final value at the time of the peak current. At this peak current, the current density distribution is more uniform for conditions with more rapid cell voltage change. The current density distribution is most non-uniform at the peak current for condition #3 (i.e., the slower rate of cell voltage change). As a result, the amount of overshoot for the average current density is lower for condition #3. These local current densities are a result of the concentration of the reacting gases, particularly oxygen under these operating conditions. The final contours of both Figs. 8 and 9 represent the local current density contours at the steady state. These contours are similar to the condition #1 (i.e., a step change in voltage).

Figs. 10 and 11 show the transient local oxygen mole fraction for incremental voltage change of conditions #2 and #3, respectively. The time steps and cell voltages

shown in Figs. 10 and 11 correspond to the currents of Figs. 8 and 9, respectively. These figures verify that the variation of local current density for the specified stoichiometry, cell voltage and time step change is due to the local oxygen concentration. The oxygen decreases from the center of membrane surface and is almost depleted toward the outlet when cell voltage is decreased to its steady state value.

4. Conclusions

A 3D time-dependent simulation of a PEMFC was shown for different rates of load change. Contours of local current density and oxygen concentration were presented and discussed. For the particular operating conditions and properties used in this study, the membrane is close to complete hydration and the results indicate that there can be current overshoot of the final cell current with the cell voltage is changed at 1 V/s from 0.7 to 0.5 V. The peak of this overshoot depends on the rate of voltage change and anode stoichiometry and the peak of current overshoot can be reduced or eliminated by decreasing the rate at which the cell voltage is changed. This overshoot behavior is a result of local non-uniformity in the current density distributions. The non-uniformity of local current density distribution depends on anode water activity and local concentration of the reacting gases, especially the oxygen concentration for the conditions of this study. These results can help our on-going studies of flow-field configuration. Design changes in these flow-fields should improve the undesirable fuel cell performance such as the current overshoot as a result of load change, and will increase the performance dramatically. Also simpler models that approximate the results may now be developed and compared with these results.

Acknowledgements

The authors gratefully acknowledge the financial support of this work by the South Carolina State University/University Transportation Center (Grant # 2000-013), the Department of Energy-EPSCoR (Cooperative Agreement # DE-FG02-91ER75666), and the Office of Naval Research (Grant # N00014-98-1-0554).

References

[1] S.-H. Kim, S. Shimpalee, J.W. Van Zee, J. Electrochem. Soc. 152 (2005) A1265–A1271.
[2] S.-H. Kim, S. Shimpalee, J.W. Van Zee, J. Power Sources 137 (2004) 43–52.
[3] S.-H. Kim, S. Shimpalee, J.W. Van Zee, J. Power Sources 135 (2004) 110–121.
[4] S. Dutta, S. Shimpalee, J.W. Van Zee, J. Appl. Electrochem. 30 (2000) 135–146.
[5] S. Dutta, S. Shimpalee, J.W. Van Zee, Int. J. Heat Mass Transfer 44/11 (2001) 2029–2042.
[6] S. Shimpalee, S. Dutta, Numer. Heat Transfer Part A 38 (2000) 111–128.
[7] W-k. Lee, S. Shimpalee, J.W. Van Zee, J. Electrochem. Soc. 150 (2003) A341–A348.
[8] S. Shimpalee, S. Greenway, D. Spuckler, J.W. Van Zee, J. Power Sources 135 (2004) 79–87.
[9] S. Um, C.Y. Wang, K.S. Chen, J. Electrochem. Soc. 147 (2000) 4485–4493.
[10] Y. Wang, C.Y. Wang, Electrochem. Acta 50 (2005) 1307–1315.
[11] T.E. Springer, T.A. Zawodzinski, S. Gottesfeld, J. Electrochem. Soc. 138 (1991) 2334–2342.
[12] D.M. Bernardi, M.W. Verbrugge, AIChE J. 37 (1991) 1151–1163.
[13] D.M. Bernardi, M.W. Verbrugge, J. Electrochem. Soc. 139 (1992) 2477–2491.
[14] T. Fuller, J. Newman, J. Electrochem. Soc. 140 (1993) 1218–1225.
[15] T. Nguyen, R. White, J. Electrochem. Soc. 140 (1993) 2178–2186.
[16] A. West, T. Fuller, J. Appl. Electrochem. 26 (1996) 557–565.
[17] J. Yi, T. Nguyen, J. Electrochem. Soc. 145 (1998) 1149–1159.
[18] J. Yi, Y. Nguyen, J. Electrochem. Soc. 146 (1999) 38–45.
[19] V. Garua, H. Liu, S. Kakac, J. AIChE 44 (1998) 2410–2422.
[20] A. Kazim, H. Liu, P. Forges, J. Appl. Electrochem. 29 (1999) 1409–1416.
[21] A. Kulikovsky, J. Divisek, A. Kornyshev, J. Electrochem. Soc. 146 (1999) 3981–3991.
[22] S. Shimpalee, W.K. Lee, H. Naseri-Neshat, J.W. S Van Zee, Proceedings of the 36th Intersociety Energy Conversion Engineering Conference, Savannah, GA, ECEC2001-ET-10, 2001, pp. 959–965.
[23] T. Zawodzinski, T. Springer, J. Davey, R. Jestel, C. Lopez, J. Valerio, S. Gottelfeld, J. Electrochem. Soc. 140 (1993) 1981–1985.
[24] T. Fuller, J. Newman, J. Electrochem. Soc. 139 (1992) 1332–1337.
[25] S.V. Patankar, Numer. Heat Transfer Fluid Flow, Hemisphere, New York, 1980.
[26] R. Bird, W. Stewart, E. Lightfoot, Transport Phenomena, John Wiley & Sons, Inc., NY, 1960.